DEEP *CHANDRA* MONITORING OBSERVATIONS OF NGC 4649. II. WIDE-FIELD *HUBBLE SPACE TELESCOPE* IMAGING OF THE GLOBULAR CLUSTERS

Jay Strader[1,2], Giuseppina Fabbiano[2], Bin Luo[2], Dong-Woo Kim[2], Jean P. Brodie[3], Tassos Fragos[2],
John S. Gallagher[4], Vassiliki Kalogera[5], Andrew King[6], and Andreas Zezas[7]

[1] Department of Physics and Astronomy, Michigan State University, East Lansing, Michigan, MI 48824, USA; strader@pa.msu.edu
[2] Harvard-Smithsonian Center for Astrophysics, Cambridge, MA 02138, USA
[3] UCO/Lick Observatory, 1156 High Street, Santa Cruz, CA 95064, USA
[4] Department of Astronomy, University of Wisconsin, Madison, WI 53706-1582, USA
[5] Center for Interdisciplinary Exploration and Research in Astrophysics (CIERA) and Department of Physics and Astronomy,
Northwestern University, 2145 Sheridan Road, Evanston, IL 60208, USA
[6] Department of Physics and Astronomy, University of Leicester, University Road, Leicester LE1 7RH, UK
[7] Physics Department, University of Crete, P.O. Box 2208, GR-710 03, Heraklion, Crete, Greece

ABSTRACT

We present g and z photometry and size estimates for globular clusters (GCs) in the massive Virgo elliptical NGC 4649 (M60) using a five-pointing *Hubble Space Telescope*/Advanced Camera for Surveys mosaic. The metal-poor GCs show a monotonic negative metallicity gradient of -0.43 ± 0.10 dex per dex in radius over the full radial range of the data, out to $\sim$24 kpc. There is evidence for substantial color substructure among the metal-rich GCs. The metal-poor GCs have typical sizes $\sim$0.4 pc larger than the metal-rich GCs out to large galactocentric distances ($\gtrsim$20 kpc), favoring an intrinsic explanation for the size difference rather than projection effects. There is no clear relation between half-light radius and galactocentric distance beyond $\sim$15 kpc, suggesting that the sizes of GCs are not generically set by tidal limitation. Finally, we identify $\sim$20 candidate ultracompact dwarfs that extend down to surprisingly faint absolute magnitudes ($M_z \sim -8.5$), and may bridge the gap between this class and "extended clusters" in the Local Group. Three of the brighter candidates have published radial velocities and can be confirmed as bona fide ultracompact dwarfs; follow-up spectroscopy will determine the nature of the remainder of the candidates.

Key words: galaxies: individual (NGC 4649) – galaxies: star clusters: general – globular clusters: general

Online-only material: color figures, machine-readable table

1. INTRODUCTION

It is well established that a large fraction of low-mass X-ray binaries in early-type galaxies are dynamically formed in globular clusters (GCs; see the review of Fabbiano 2006). These sources are preferentially found in red metal-rich GCs and in those clusters with the highest interaction rates, which occur in the clusters with small radii and large stellar densities (e.g., Kundu et al. 2002; Pooley et al. 2003). Therefore, precision photometry and structural parameters for GCs are necessary to properly interpret X-ray observations of nearby elliptical galaxies.

To complement new deep, multi-epoch *Chandra* X-ray observations of the massive Virgo elliptical NGC 4649 (M60; VCC 1978), we have obtained *Hubble Space Telescope*/Advanced Camera for Surveys (*HST*/ACS) pointings that tile most of the *Chandra* field of view. The *Chandra* catalog is presented in B. Luo et al. (2012, in preparation). Future papers will discuss the properties of low-mass X-ray binaries in NGC 4649, specific interesting systems, and other topics.

This paper derives properties of GCs (photometry and sizes) in the *HST*/ACS data and points out several interesting features of the GC system itself, in the context of their use as tracers of the formation and evolution of massive galaxies (Brodie & Strader 2006). The most notable feature of this data set, compared to the voluminous set of previous *HST* imaging studies of massive ellipticals, is the areal coverage: our five ACS pointings, combined with an archival pointing of equivalent depth, cover $\sim$60 arcmin², with near-complete azimuthal coverage to

projected radii $\gtrsim$20 kpc. These data allow the study of GC colors and effective radii as a function of galactocentric radius over a radial range not usually possible with *HST* data, unless one studies more distant galaxies. Among the scientific questions that can be addressed is whether the well-known size difference between blue and red GCs is due primarily to projection effects (e.g., Larsen & Brodie 2003), and if metallicity gradients are present within the individual GC subpopulations (Harris 2009; Forbes et al. 2011). The added areal coverage also aids in the hunt for uncommon objects, such as candidate ultracompact dwarf galaxies (Brodie et al. 2011).

2. DATA REDUCTION AND ANALYSIS

2.1. Basic Reductions

The ACS observations were arranged in a five-pointing mosaic with slight overlap around a central archival pointing from the ACS Virgo Cluster Survey (Côté et al. 2004). Together, these data cover the sensitive portion of the *Chandra* ACIS field of view, excluding the nearby spiral NGC 4647. Each pointing consists of 888 s of total exposure time in F475W and 1278 s in F850LP (henceforth called g and z), with each exposure split using a simple line dither to cover the ACS chip gap. The spatial coverage of the data is shown in Figure 1.

ACS observations taken after the most recent *HST* servicing mission require additional processing steps that, at the time of these reductions, were not yet incorporated into the standard pipeline. We started with the .flt files that have been bias- and dark-corrected and flat-fielded. First, we corrected the bias

<div align="center">

Table 1
Globular Cluster Candidates in NGC 4649

</div>

ID	R.A. (J2000) (deg)	Decl. (J2000) (deg)	g (mag)	err (mag)	z (mag)	err (mag)	$g-z$ (mag)	err (mag)	$r_{h,g}$ (pc)	err (pc)	$r_{h,z}$ (pc)	err (pc)	$r_{h,avg}$ (pc)	err (pc)	VCS?[a]
A3	190.9508006	11.5432966	21.004	0.011	19.555	0.011	1.449	0.016	2.18	0.16	2.23	0.16	2.20	0.11	...
A4	190.9257483	11.5636199	21.512	0.010	20.220	0.010	1.284	0.014	2.23	0.23	2.39	0.24	2.30	0.17	Y
A5	190.9359288	11.5543245	21.901	0.010	20.379	0.009	1.532	0.013	2.59	0.19	2.17	0.16	2.34	0.12	Y
A6	190.9950621	11.5679435	21.539	0.012	20.413	0.012	1.126	0.017	2.30	0.24	2.18	0.22	2.24	0.16	...
A7	190.9738846	11.5381531	21.813	0.012	20.444	0.012	1.369	0.017	2.85	0.21	2.87	0.21	2.86	0.15	...
A8	190.9426739	11.5595950	21.971	0.011	20.475	0.011	1.500	0.015	1.94	0.20	1.81	0.18	1.87	0.14	Y
A11	190.9683138	11.5508885	21.593	0.012	20.587	0.013	1.006	0.018	3.71	0.38	2.89	0.30	3.20	0.23	...
A12	190.9474641	11.5785513	21.706	0.012	20.627	0.013	1.079	0.018	2.16	0.22	2.03	0.21	2.09	0.15	...
A13	190.9353218	11.5549610	22.132	0.012	20.651	0.013	1.456	0.017	2.00	0.21	2.14	0.22	2.07	0.15	Y
A14	190.9727156	11.5384375	22.017	0.013	20.729	0.013	1.288	0.018	2.36	0.18	2.03	0.15	2.17	0.11	...

Notes. [a] Whether the object is present in the GC catalog of Jordán et al. (2009).

(This table is available in its entirety in a machine-readable form in the online journal. A portion is shown here for guidance regarding its form and content.)
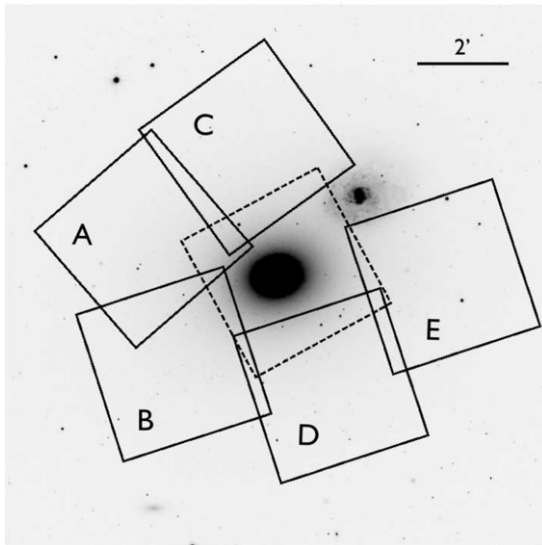
Figure 1. SDSS DR7 mosaic image of NGC 4649 (and the foreground spiral NGC 4647), with the approximate location of our ACS pointings superposed (solid lines). The archival ACS Virgo Cluster Survey central pointing is shown with dotted lines.

striping using the PyRaf routine provided by STScI.[8] Next, we corrected for the ACS charge transfer efficiency losses using the STScI routine that implements the algorithm of Anderson & Bedin (2010).[9] To reject cosmic rays, we ran L.A.Cosmic (van Dokkum 2001) on the resulting images using relatively conservative criteria. Finally, these processed images were combined using MultiDrizzle in PyRaf to produce distortion-corrected mosaics for photometry for each filter and pointing.

Before performing photometry, we used moderately bright, unsaturated objects to shift the astrometry of each image onto the standard system of the Sloan Digital Sky Survey Data Release 7 (Abazajian et al. 2009).

2.2. Cluster Detection and Photometry

We used SExtractor (Bertin & Arnouts 1996) to produce initial candidate lists for photometry. Sources were selected on median-subtracted images, using an optimal weight map, with a low threshold (1.5σ) and a requirement of at least five

connected pixels. Separate candidate lists for the g and z images were matched to within 2 pixels ($0.\!''1$).

We performed aperture photometry on this matched candidate list using a 5 pixel aperture. GCs at the distance of NGC 4649 are marginally resolved and larger clusters will have a greater fraction of their total flux distributed beyond a fixed aperture. We corrected the 5 pixel base magnitudes to 10 pixel ($0.\!''5$) magnitudes using size-dependent aperture corrections, calculated as described below in Section 2.3.1. These magnitudes were then corrected to a nominal infinite aperture using the values from Sirianni et al. (2005). For the largest objects, an additional correction for light beyond the ($0.\!''5$) aperture was also required. Finally, these magnitudes were corrected for foreground reddening using the maps of Schlegel et al. (1998) as updated by Peek & Graves (2010). All magnitudes are in the AB system.

We have 234 GCs in common with the catalog of Jordán et al. (2009; these data were also discussed in Peng et al. 2006 and Mieske et al. 2006). The median difference in both g and z magnitudes between this catalog and our measurements is 0.01 mag. The median difference in $g-z$ is 0.002 mag. These comparisons show that our photometry is in excellent agreement with the published values, and all of the measurements can be compiled into a self-consistent photometric catalog. This catalog is given in Table 1. We assume a distance of 16.5 Mpc to NGC 4649 (Blakeslee et al. 2009) for the paper.

2.3. Cluster Sizes

We measured half-light radii using *ishape* (Larsen 1999). Since cluster concentration c cannot be reliably measured except for the most luminous clusters,[10] we used a fixed value of $c = 30$ for all objects. For most clusters we used a fitting radius of 5 pixels (equivalent to 20 pc). For the largest clusters ($r_h > 10$ pc), we increased the fitting radius in 1 pixel increments as necessary so that it was always at least twice as large as the measured effective radius.

Harris (2009) argues that measurements of r_h can only be made with confidence for objects with S/N > 50. For clusters of typical size and background, this value corresponds to magnitude limits of $z < 23$ and $g < 24$; we restrict our size measurements to these limits. In Table 1, we list the individual g and z r_h values as well as a weighted average of the two bands.

There are 703 objects with size measurements in both g and z. The median difference in r_h, in the sense of $r_{h,g} - r_{h,z}$,

[10] $c = r_t/r_0$ for tidal radius r_t and King radius r_0.
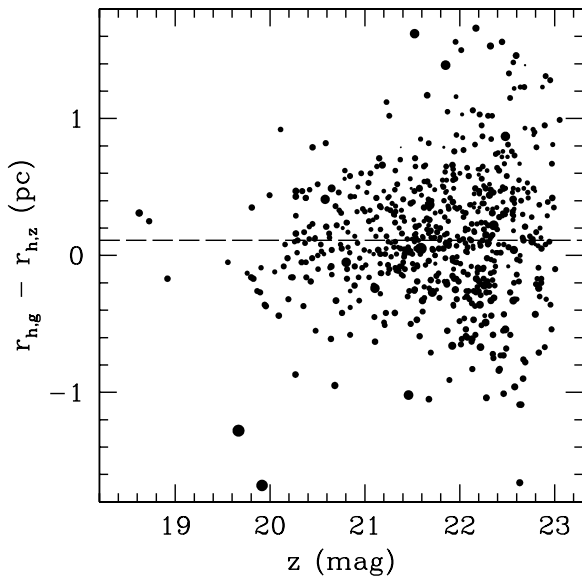
Figure 2. Differences between our r_h measurements in g and z as a function of z magnitude, with the point size proportional to the logarithm of r_h in z. The median difference is marked with a dashed line.
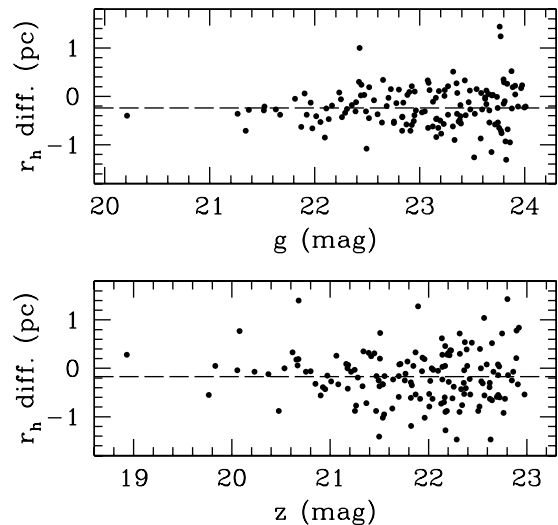

Figure 3. Differences between our r_h estimates and those from Jordán et al. (2009), in the sense of us–them, as a function of g and z magnitude. The median difference is marked with a dashed line for each filter.

is 0.11 pc, indicating good agreement between the filters. Figure 2 shows a comparison between these size estimates. The random uncertainties in the sizes, given the assumed model (King profiles with fixed $c = 30$) were estimated by comparing clusters that fell within the boundaries of more than one pointing. Assuming that the random uncertainties in r_h in each pointing are Gaussian and identical, the distribution of pairwise r_h differences, considered separately for each filter, should have a variance that is twice that of the individual measurements. For each filter, we estimated this quantity in magnitude bins and then fit a smooth exponential function to the data. These fits were used to assign uncertainties for each r_h estimate.

For an individual filter, we find typical uncertainties of 10% for more luminous objects and 20% for the faintest clusters for which we report sizes. Previous studies using ACS data suggest that the systematic uncertainties in size measurements from point-spread function (PSF) modeling for GCs at the distance of NGC 4649 are ∼0.4 pc, or ∼20% for a typical cluster (Spitler et al. 2006; Harris 2009). The r_h values in Table 1 include only the random measurement errors.

As with the photometry, we can compare our estimates of r_h to those of Jordán et al. (2009), after converting their published r_h values from angular to physical units using the assumed distance of 16.5 Mpc. In the median, our values are smaller by 0.25 ± 0.04 pc and 0.17 ± 0.07 in g and z, respectively. These amount to systematic differences of ∼10%, well within the overall systematic uncertainty of size estimates from PSF modeling. In particular, Jordán et al. (2009) state systematic uncertainties in r_h of ∼0″.005 (0.4 pc). The median differences in r_h in both g and z are well within this estimate of the systematic uncertainty in the measurements. We compare r_h measurements for GCs in common between this study and Jordán et al. (2009) in Figure 3.

2.3.1. Use in Aperture Corrections

Our cluster r_h estimates form the basis for size-dependent aperture corrections to the photometry. These were measured by convolving our empirical PSFs with King models of fixed concentration ($c = 30$) and varying r_h. We define our basic

aperture corrections from a radius of 5 pixels (0″.25) to 10 pixels (0″.5). For the largest clusters (with $r_h > 6$ pc), making up ∼3% of the total sample, an additional aperture correction for light falling outside of the 10 pixel radius is required. Representative corrections in g are -0.08 and -0.30 mag for $r_h = 10$ and 20 pc, respectively. Because of the lower signal-to-noise ratio (S/N) of the empirical PSF in its outer regions, these extra corrections are less well constrained, and the total magnitudes of the largest clusters in our sample are less precise. However, these corrections have a minimal effect on the cluster colors (see below).

Uncertainty in the value of r_h for a particular cluster has a minimal effect on the $g - z$ color. For example, over the range 1–10 pc, the maximum deviation from the median correction is only 0.003 mag in $g - z$. For typical size uncertainties of 0.5–1 pc, the correction is utterly negligible. This point has been made before in the context of discussions of the "blue tilt" of luminous metal-poor GCs (Jordán et al. 2009).

Uncertainties in sizes can have a larger effect on the total magnitudes of GCs. For clusters of typical size (2–3 pc), a 20% size uncertainty translates into about 0.01 mag in luminosity. For larger clusters, the effect can be much more significant, corresponding to 0.04–0.05 mag for a cluster with $r_h = 10$ pc. However, few of the GCs are this large, and none of our conclusions depend strongly on the precise cluster luminosities in any case.

2.4. Cluster Selection

GCs were selected using these basic criteria: (1) $z < 24$; (2) $0.5 < g - z < 2.0$. Any objects whose sizes were consistent with zero were presumed to be foreground stars and were discarded. No upper size limit was used because of the presence of candidate ultracompact dwarf galaxies (see Section 3.3); in any case, few objects with sizes >10 pc are present (22 in the whole catalog). The faint z limit extends ∼1.3 mag fainter than the turnover of the GC luminosity function at $z \sim 22.7$ (Jordán et al. 2007). After these cuts, a visual inspection was used to remove obvious background galaxies.

Objects in the main body of the projected spiral NGC 4647 were also removed, though more distant GCs in this galaxy may remain in the catalog. We can roughly estimate this
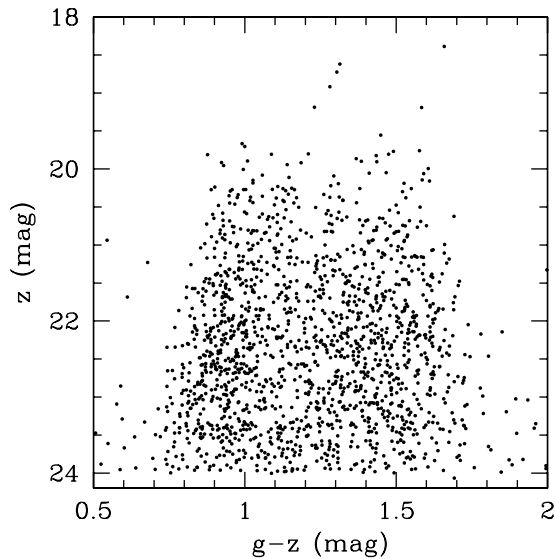
Figure 4. z vs. $g - z$ color–magnitude diagram of GCs in NGC 4649. The standard blue and red GC subpopulations are visible, as well as a color–luminosity relation for the brighter blue (metal-poor) GCs.

Figure 5. $g - z$ vs. projected galactocentric distance (R_G) for GCs in NGC 4649. The overplotted blue squares and red triangles are the peak colors for the metal-poor and metal-rich subpopulations. There is a radial gradient in color (metallicity) for the metal-poor GCs, but no clear trend for the metal-rich GCs. (A color version of this figure is available in the online journal.)

contamination as follows: a galaxy with $M_V \sim -19.9$ (de Vaucouleurs et al. 1991) should have $\sim$25–50 GCs brighter than the turnover, about half of which are inside the excluded central $\sim$4–5 kpc (Brodie & Strader 2006). Further, our image mosaic only covers the half of the galaxy toward NGC 4649. Therefore, we expect that perhaps 5–10 objects in our catalog are GCs associated with NGC 4647.

The area covered is shown graphically in Figure 1, and is divided into our pointings (A)–(E) and the central ACS Virgo Cluster Survey pointing, denoted "J" in our catalog.

About 8% of our GCs were present in multiple pointings, and the photometry and size measurements for these objects are averages of the individual values. In addition, 20% of the objects are present in the Jordán et al. (2009) catalog. For these objects, given the agreement between our photometric measurements, we simply average the magnitudes. For consistency, because of the small but significant differences in the size estimates, we do not average together the sizes, but solely use our estimates. We add the rest of the Jordán et al. (2009) candidates, applying the selection criteria above, into a master catalog with 1603 GCs. Of this total, 1120 have photometry from our new data.

3. RESULTS

Figure 4 shows the $g - z$ versus z color–magnitude diagram (CMD) of GCs in NGC 4649. The basic features of the CMD are similar to those observed in previous *HST*/ACS studies of NGC 4649. Evident features include the standard bimodal color distribution in $g - z$ of blue metal-poor and red metal-rich GCs, and evidence for the "blue tilt": a correlation between color and magnitude for the most luminous blue GCs (Strader et al. 2006; Harris et al. 2006; Mieske et al. 2006). We do not dwell on these established facts, but focus on the features of the GC system that can be studied with our improved radial coverage.

3.1. Radial Variations in Color

The $g - z$ colors are plotted against the projected galacto-centric distance in Figure 5. We overplot the peak colors of the blue and red subpopulations, calculated from density estimates
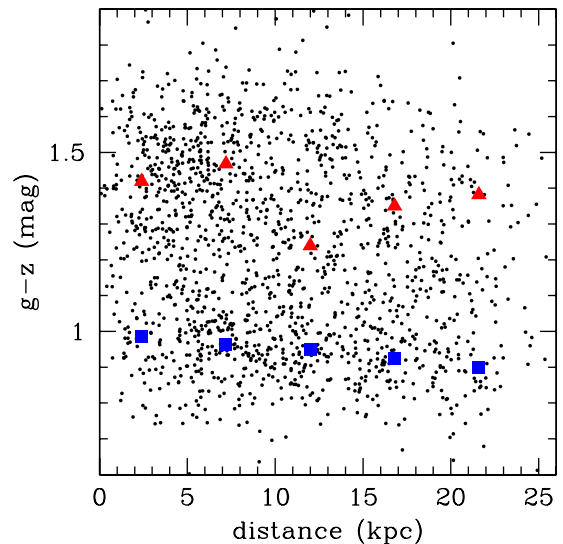
using a Gaussian kernel of 0.05 mag and $1'$ (4.8 kpc) bins.[11] For these density estimates, only GCs with $23 < z < 21$ are used, to minimize the effects of the blue tilt and of faint contaminants.

The metal-poor GCs have a monotonic color gradient with radius: -0.021 ± 0.001 mag arcmin^{-1}, corresponding to a negative metallicity gradient of -0.43 ± 0.10 dex per dex in radius (assuming the $g - z$ to [Fe/H] conversion of Peng et al. 2006). The outer edge of our data (at $\sim$24 kpc) is close to the typical "break radius" observed in the metal-poor GC systems of some other galaxies, beyond which the gradient flattens to near-zero (Harris 2001; Forbes et al. 2011), although this break appears to occur by $\sim$15 kpc in M87 (Strader et al. 2011). Data at larger radii will be necessary to look for an edge to the gradient in NGC 4649.

We note that our measured gradient is somewhat steeper than found by Harris (2009) for metal-poor GCs in a sample of more distant brightest cluster galaxies. It not clear how comparable the two measurements are, as Harris necessarily restricted his fit to luminous GCs ($M_i < -9$) that are more likely to be affected by the blue tilt, which is known to vary with radius (Mieske et al. 2010). Indeed, if we restrict our analysis to GCs with $z < 22$, yielding a luminosity cut similar to that of Harris (2009), there is no significant evidence for a metallicity gradient among the metal-poor GCs in NGC 4649. We conclude that the blue tilt can have an important effect on measured gradients and that conclusions based on the most luminous GCs may be biased.

There is minimal evidence for a metallicity gradient among the metal-rich GCs. While the mean peak color of the innermost two bins is $\sim$0.08 mag redder in $g - z$ than the outermost two bins, there appears to be significant color substructure at all radii; at radii between $2'$ and $3'$ (9.6–14.4 kpc), there is no well-defined red peak at all. This substructure suggests the presence of GCs from accretion events that have not yet been fully phase mixed into NGC 4649.

Both the monotonic metal-poor GC gradient and the substruc-ture in the red peak are evident in the density plots themselves,

---

[11] We use this method, rather than the common Gaussian mixture modeling, because it is less sensitive to outliers.
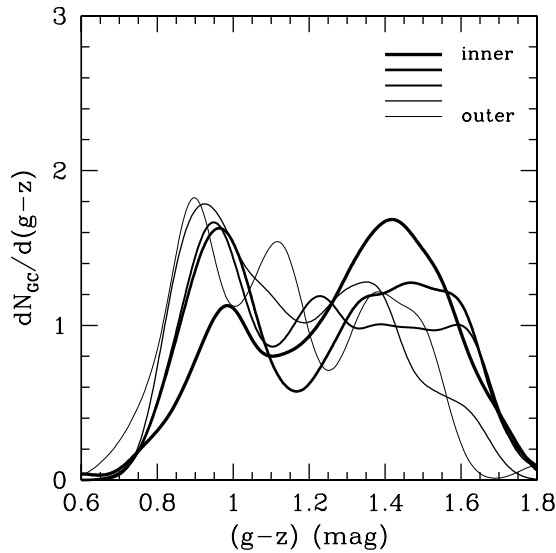
Figure 6. Kernel density estimates of the color distribution of GCs in NGC 4649 with $23 < z < 21$ as a function of projected galactocentric distance, with thicker lines representing more central distances. A fixed Gaussian kernel of 0.05 mag was used, and the mean distances plotted run from 0′.5 (2.4 kpc) to 4′.5 (21.6 kpc) in 1′ (4.8 kpc) bins. The metal-poor peak is symmetric and shows the negative metallicity gradient discussed in the text, while the metal-rich peak shows significant color substructure at all distances.

which are shown in Figure 6. These findings are remarkably similar to observations of GCs in the giant elliptical galaxies M87 (Strader et al. 2011; see their Figure 9) and NGC 1407 (Forbes et al. 2011; see their Figure 2). These data provide compelling evidence that the blue GC gradient and red GC substructure exist in the GC systems of many massive early-type galaxies.

The inner blue GC gradient appears to have a similar slope among the galaxies studied so far. The situation for the red GCs is less certain—while substructure in color appears ubiquitous, the presence of a red GC gradient is only clear in some galaxies, such as NGC 1407 (Forbes et al. 2011). In M87, Strader et al. (2011) argue that there is an extended, kinematically distinct intermediate-color subpopulation of GCs, separate from the standard red subpopulation, that causes the appearance of a gradient in the red GC color. These results suggest that care should be taken in the interpretation of simple two-population fits to GC color distributions.

3.2. Radial Variations in Half-light Radii

Numerous previous studies of early-type galaxies, including NGC 4649, have shown that the metal-poor GCs are 0.3–0.5 pc larger than the metal-rich GCs (Kundu & Whitmore 1998; Larsen et al. 2001; Jordán et al. 2005), and have debated whether this observation is primarily due to intrinsic size differences or to projection effects (Larsen & Brodie 2003; Jordán 2004). The former theory predicts a similar difference in sizes between the two subpopulations at all galactocentric distances; in the latter theory the size difference should disappear at larger projected distances.

To create a sample of r_h estimates that is as clean as possible, we imposed several criteria. First, GCs with $z < 21$ were excluded, since the brighter GCs are systematically larger (see Section 3.3). Next, we excluded objects with $z > 22.5$, to reduce contamination that might preferentially affect the statistics in the outermost bins. We also only used sizes from our new data, due to the small systematic difference with Jordán et al.
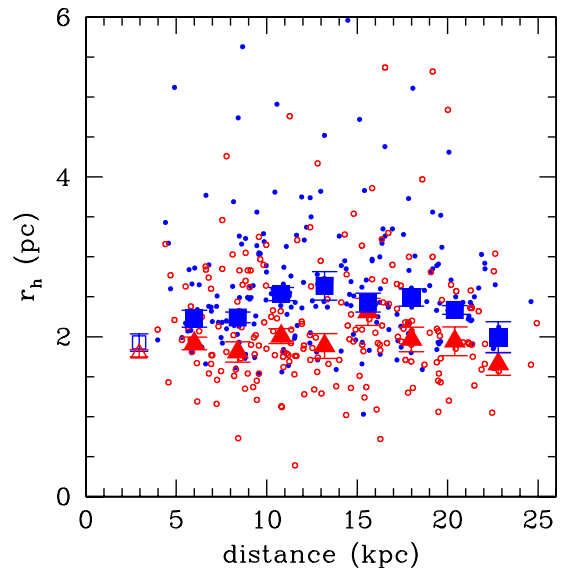
Figure 7. r_h vs. projected galactocentric distance (R_G) for GCs in NGC 4649, using the selection criteria described in the text. Small blue filled circles are individual blue GCs and open circles are red GCs. The overplotted blue squares and red triangles are the modes of the metal-poor and metal-rich subpopulations. The blue GCs appear larger at all distances, and show a mild increase in r_h with distance in the inner bins. At greater distances, both subpopulations show flat or declining r_h. The single open blue square and red triangle represent GCs from Jordán et al. (2009) within 1′, using the same selection criteria, and including the systematic offset in r_h stated in Section 2.3.

(A color version of this figure is available in the online journal.)

(2009) as documented above (and, in general, care should be taken when combining r_h estimates from different studies). This restricts the estimates to projected radii $\gtrsim 5$ kpc.

In Figure 7, we plot the half-light radii of GCs that pass these selection criteria as a function of projected galactocentric distance. Overplotted are the modes of density estimates using a fixed Gaussian kernel of 0.25 pc, split into blue and red GC subpopulations at $g - z = 1.18$. This plot shows two interesting features. First, the metal-poor GCs are larger than the metal-rich GCs at all galactocentric distances, and the difference in r_h (~ 0.4 pc) does not appear to vary with distance over the range studied. This observation strongly disfavors the "projection" hypothesis and suggests that the half-light radii of metal-poor GCs are intrinsically larger than metal-rich GCs. For reference, we have also plotted the blue and red r_h modes for GCs from Jordán et al. (2009) within 1′.

The other interesting feature of this plot is the run of r_h with galactocentric distance. For the metal-rich GCs there is evidently no relationship over the range 5–25 kpc. For the inner ($\lesssim 15$ kpc) metal-poor GCs there is marginal evidence for a correlation of the form: $r_h \propto R_G^{0.14 \pm 0.06}$, where R_G is the projected galactocentric distance. This slope agrees with that from previous observations of other galaxies (Spitler et al. 2006; Gómez & Woodley(2007); Harris 2009; Harris et al. 2010), though at lower significance. However, at distances $\gtrsim 15$ kpc, the typical r_h is flat or declining.

The weak inner correlation between r_h and R_G and flat outer trend are consistent with another recent wide-field *HST*/ACS survey of GCs in the giant elliptical NGC 1399 (Paolillo et al. 2011). Thus there is mounting evidence that, at least in some massive galaxies, the r_h–R_G relation is confined to the inner regions and does not exist at all galactocentric radii. This suggests that the sizes of GCs are not generically set by tidal
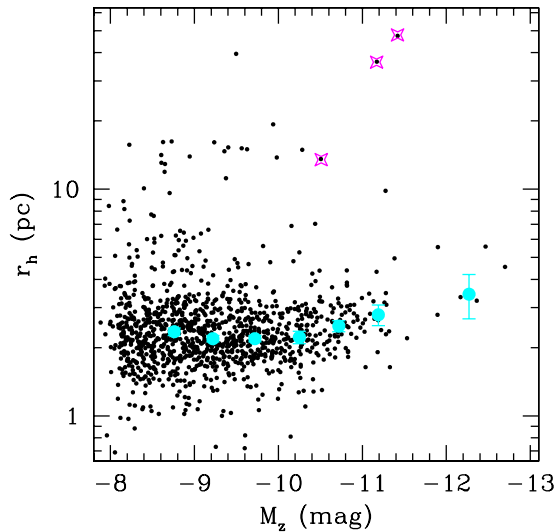
Figure 8. r_h vs. M_z for GCs in NGC 4649. There is a trend of increasing r_h for the most luminous GCs ($M_z \lesssim -10$) and a large population of candidate ultracompact dwarf galaxies with $r_h > 10$ pc, extending down to surprisingly faint magnitudes. Three spectroscopically confirmed ultracompact dwarfs are marked with magenta stars. The large cyan circles are median r_h of objects with $r_h < 10$ pc in 0.5 mag bins, from $M_z = -8.5$ to -11.5, with uncertainties by bootstrapping. To compensate for small numbers, the final bin is contains all objects from $M_z = -11.5$ to -13.

(A color version of this figure is available in the online journal.)

Table 2
Ultracompact Dwarf Candidates in NGC 4649

ID	M_z (mag)	$g - z$ (mag)	r_h (pc)	Distance[a] (kpc)
D68	−11.42	0.99	47.4	13.1
A32	−11.17	0.92	36.5	6.2
C28	−10.51	0.93	13.6	11.5
J67	−11.28	0.88	9.8	1.8
C42	−10.28	0.92	14.9	15.4
A51	−9.98	1.66	13.8	12.9
A78	−9.94	1.56	19.3	14.2
C84	−9.63	1.59	15.0	8.8
A98	−9.56	1.26	15.1	18.7
A155	−9.50	1.03	39.5	6.1
E86	−9.40	0.61	15.3	24.9
B139	−9.38	0.95	11.2	12.6
A122	−9.36	1.60	14.7	9.0
E91	−9.24	1.69	16.1	9.3
E123	−8.94	1.85	13.9	13.0
A209	−8.73	1.01	16.2	19.5
A205	−8.65	1.23	12.9	22.5
A701	−8.65	1.73	11.9	6.2
A225	−8.63	1.04	16.1	6.9
D243	−8.61	1.60	13.1	10.2
A221	−8.60	1.33	14.1	18.5
E161	−8.40	1.00	10.1	9.7
D312	−8.22	0.83	15.7	18.7

Notes. Spectroscopically confirmed objects are listed first.
[a] Projected galactocentric distance.

limitation (see also Brodie et al. 2011; Webb et al. 2012). We note that there may yet be galaxies for which the tidal limitation scenario is relevant, for example, Blom et al. (2012) report a steep relation $r_h \propto R_G^{0.49}$ for GCs in the elliptical NGC 4365, which is similar to the relation in the Milky Way (e.g., van den Bergh et al. 1991).

3.3. Ultracompact Dwarf Galaxies

Figure 8 shows the r_h estimates of GCs in NGC 4649 as a function of M_z. The sizes are plotted logarithmically as the range is large. We see the correlation between r_h and cluster luminosity for the most massive GCs that has been observed in many galaxies (e.g., Haşegan et al. 2005; Evstigneeva et al. 2008; Harris 2009; Harris et al. 2010). Many of these papers have interpreted this trend as a continuous size–luminosity relationship extending from GCs to much larger ultracompact dwarfs, and have defined the latter class solely by luminosity. Brodie et al. (2011) argue instead that, rather than a continuous sequence of compact massive objects, there are two essentially parallel sequences separating GCs with $r_h \lesssim 10$ pc and ultracompact dwarfs with $r_h \gtrsim 10$ pc over a wide range of luminosities.

The NGC 4649 data in Figure 8 are consistent with this classification: considering objects with $r_h < 10$ pc, the median size is constant at 2–3 pc for faint GCs, increasing for $M_z \lesssim -10$, and a monotonic trend continuing to the most luminous GCs at $M_z \sim -13$. As this trend is continuous with luminosity, we see no reason to classify these most massive objects, with $r_h \sim 3$–5 pc, as anything other than very luminous star clusters. Such GCs do not appear to exist around M87—all of the objects around M87 of this luminosity are >10 pc in size (Brodie et al. 2011; Strader et al. 2011)—although there are isolated examples in the literature, typically in galaxy clusters (Mieske et al. 2007; Misgeld & Hilker 2011; Norris & Kannappan 2011; Chiboucas et al. 2011).

There is a parallel sequence of nearly 20 objects with $r_h \sim 10$–20 pc from $M_z \sim -8.5$ to -11. The faintest of these objects bridge the gap between the (poorly defined) faint end of the ultracompact dwarf and the "extended clusters" discovered in M31 and other Local Group galaxies (e.g., Huxor et al. 2011; Hwang et al. 2011). The brightest object in this size range, C28, has been confirmed as a member of NGC 4649 by previous spectroscopy (Lee et al. 2008) and is marked in Figure 8. Additional spectroscopy is necessary before further conclusions can be drawn; it is likely that a subset of these objects are background galaxies. For example, the candidates with outlying colors (e.g., E86, E123) have a larger chance of being background objects.

In addition to these moderately extended sources, there are three very large ($\sim$40 pc) objects, two of which would fall in the "classic" ultracompact dwarf luminosity range $M_z \lesssim -11$. All objects with $r_h \gtrsim 10$ pc are listed as ultracompact dwarf candidates in Table 2. These data emphasize the conclusion that luminosity criteria alone are insufficient to classify objects as GCs or ultracompact dwarfs. Two of the three (A32 and D68) have also been spectroscopically confirmed in the literature (Lee et al. 2008; Pierce et al. 2006) and thus can be recognized as bona fide ultracompact dwarfs. They are specially marked in Figure 8.

Ultracompact dwarfs have been discovered primarily at the centers of large galaxy clusters (e.g., Drinkwater et al. 2003), though examples exist in a range of environments (Norris & Kannappan 2011). At least some ultracompact dwarfs are thought to be the remnant nuclei of tidally threshed dwarf galaxies, and this process can occur most efficiently in high density environments. NGC 4649 sits at the center of a moderately massive group (Humphrey et al. 2006) in the larger context of Virgo. Given that only a small fraction of the halo radius of the galaxy

has been surveyed, the confirmation of a significant number of the candidates would show that ultracompact dwarfs can form efficiently in lower-mass environments.

4. SUMMARY

We have presented photometry and half-light radii for GCs in an *HST* mosaic of the third most massive elliptical in the Virgo cluster, NGC 4649. The improved radial coverage compared to most *HST* studies of nearby galaxies reveals several interesting features, including significant color substructure in the metal-rich GC subpopulation at all distances and a flat or declining r_h gradient beyond ∼15 kpc. The metal-poor GCs are larger than the metal-rich GCs at all radii, implying that the size difference between the two subpopulations is intrinsic rather than due to projection effects. We have also identified a large population ($\gtrsim$20) of candidate ultracompact dwarf galaxies that may extend to unusually faint luminosities. It is clear that the radial properties of GC systems in massive galaxies deserve further study with the high precision of *HST*.

REFERENCES

Abazajian, K. N., Adelman-McCarthy, J. K., Agüeros, M. A., et al. 2009, ApJS, 182, 543
Anderson, J., & Bedin, L. R. 2010, PASP, 122, 1035
Bertin, E., & Arnouts, S. 1996, A&AS, 117, 393
Blakeslee, J. P., Jordán, A., Mei, S., et al. 2009, ApJ, 694, 556
Blom, C., Spitler, L. R., & Forbes, D. A. 2012, MNRAS, 420, 37
Brodie, J. P., Romanowsky, A. J., Strader, J., & Forbes, D. A. 2011, AJ, 142, 199
Brodie, J. P., & Strader, J. 2006, ARA&A, 44, 193
Chiboucas, K., Tully, R. B., Marzke, R. O., et al. 2011, ApJ, 737, 86
Côté, P., Blakeslee, J. P., Ferrarese, L., et al. 2004, ApJS, 153, 223
de Vaucouleurs, G., de Vaucouleurs, A., Corwin, H. G., Jr., et al. 1991, Third Reference Catalogue of Bright Galaxies (New York: Springer)
Drinkwater, M. J., Gregg, M. D., Hilker, M., et al. 2003, Nature, 423, 519
Evstigneeva, E. A., Drinkwater, M. J., Peng, C. Y., et al. 2008, AJ, 136, 461
Fabbiano, G. 2006, ARA&A, 44, 323
Forbes, D. A., Spitler, L. R., Strader, J., et al. 2011, MNRAS, 413, 2943
Gómez, M., & Woodley, K. A. 2007, ApJ, 670, L105
Harris, W. E., Spitler, L. R., Forbes, D. A., & Bailin, J. 2010, MNRAS, 401, 1965
Harris, W. E. 2009, ApJ, 699, 254
Harris, W. E., Whitmore, B. C., Karakla, D., et al. 2006, ApJ, 636, 90
Harris, W. E. 2001, in Saas-Fee Advanced Course 28: Star Clusters, ed. L. Labhardt & B. Binggeli (Berlin: Springer), 223
Haşegan, M., Jordán, A., Côté, P., et al. 2005, ApJ, 627, 203
Humphrey, P. J., Buote, D. A., Gastaldello, F., et al. 2006, ApJ, 646, 899
Huxor, A. P., Ferguson, A. M. N., Tanvir, N. R., et al. 2011, MNRAS, 414, 770
Hwang, N., Lee, M. G., Lee, J. C., et al. 2011, ApJ, 738, 58
Jordán, A., Peng, E. W., Blakeslee, J. P., et al. 2009, ApJS, 180, 54
Jordán, A., McLaughlin, D. E., Côté, P., et al. 2007, ApJS, 171, 101
Jordán, A., Côté, P., Blakeslee, J. P., et al. 2005, ApJ, 634, 1002
Jordán, A. 2004, ApJ, 613, L117
Kundu, A., Maccarone, T. J., & Zepf, S. E. 2002, ApJ, 574, L5
Kundu, A., & Whitmore, B. C. 1998, AJ, 116, 2841
Larsen, S. S., & Brodie, J. P. 2003, ApJ, 593, 340
Larsen, S. S., Brodie, J. P., Huchra, J. P., Forbes, D. A., & Grillmair, C. J. 2001, AJ, 121, 2974
Larsen, S. S. 1999, A&AS, 139, 393
Lee, M. G., Hwang, H. S., Park, H. S., et al. 2008, ApJ, 674, 857
Misgeld, I., & Hilker, M. 2011, MNRAS, 414, 3699
Mieske, S., Jordán, A., Côté, P., et al. 2010, ApJ, 710, 1672
Mieske, S., Hilker, M., Jordán, A., Infante, L., & Kissler-Patig, M. 2007, A&A, 472, 111
Mieske, S., Jordán, A., Côté, P., et al. 2006, ApJ, 653, 193
Norris, M. A., & Kannappan, S. J. 2011, MNRAS, 414, 739
Paolillo, M., Puzia, T. H., Goudfrooij, P., et al. 2011, ApJ, 736, 90
Peek, J. E. G., & Graves, G. J. 2010, ApJ, 719, 415
Peng, E. W., Jordán, A., Côté, P., et al. 2006, ApJ, 639, 95
Pierce, M., Bridges, T., Forbes, D. A., et al. 2006, MNRAS, 368, 325
Pooley, D., Lewin, W. H. G., Anderson, S. F., et al. 2003, ApJ, 591, L131
Schlegel, D. J., Finkbeiner, D. P., & Davis, M. 1998, ApJ, 500, 525
Sirianni, M., Jee, M. J., Benítez, N., et al. 2005, PASP, 117, 1049
Spitler, L. R., Larsen, S. S., Strader, J., et al. 2006, AJ, 132, 1593
Strader, J., Brodie, J. P., Spitler, L., & Beasley, M. A. 2006, AJ, 132, 2333
Strader, J., Romanowsky, A. J., Brodie, J. P., et al. 2011, ApJS, 197, 33
van den Bergh, S., Morbey, C., & Pazder, J. 1991, ApJ, 375, 594
van Dokkum, P. G. 2001, PASP, 113, 1420
Webb, J. J., Sills, A., & Harris, W. E. 2012, ApJ, 746, 93